Chemical and Structural Insights of the Nano Organo–Mineral Interfaces in Growing Abalone Nacre

Widad Ajili, Marta de Frutos, Imène Estève, Marie Albéric, Nicolas Menguy, Karim Benzerara, Antonio Checa, Stéphanie Auzoux-Bordenave, Thierry Azaïs, Nadine Nassif

Chemical and Structural Insights of the Nano Organo−Mineral Interfaces in Growing Abalone Nacre

Published as part of the Chemistry of Materials virtual special issue "In Honor of Prof. Clement Sanchez".

Widad Ajili, Marta de Frutos, Imène Estève, Marie Albéric, Nicolas Menguy, Karim Benzerara, Antonio Checa, Stéphanie Auzoux-Bordenave,* Thierry Azaïs,* and Nadine Nassif*

Cite This: *Chem. Mater.* 2023, 35, 6059−6069

ABSTRACT: Characterizing the nano organo−mineral interfaces in nacre is of primary importance to understand the processes of nucleation, growth, orientation, and organization of the aragonite tablets. Here, we investigated these different interfaces in growing nacre of abalone *Haliotis tuberculata* shell using a combination of advanced techniques, i.e., focused ion beam milling coupled with field emission gun scanning electron microscopy, high-resolution transmission electron microscopy, scanning transmission X-ray microscopy, and electron energy loss spectroscopy. We show the presence of "globules"-like organic-rich inclusions within the center of each tablet that extend from one tablet to another through mineral bridges surrounded by organics. These structures may control the growth of the columnar stacking of tablets supporting different findings from the literature. In the lateral growing surface of the tablets, we reveal the presence of a thick organic domain rich in calcium but deficient in carbonate ions strengthening the idea that calcium-binding acidic proteins are involved in tablet's lateral growth. Overall, this work emphasizes the importance of nanoscale chemical and structural analysis of the organo−mineral interfaces in growing nacre, allowing in particular for the discrimination between organic and inorganic carbons.

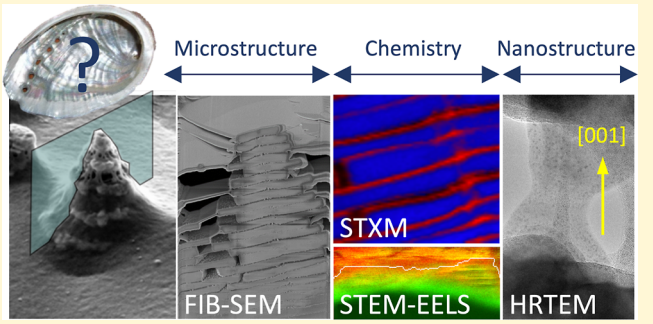

1. INTRODUCTION

Nacre is one of the most fascinating biological hybrid materials due to its remarkable architecture organized at different length scales and, as such, has been studied for more than 150 years.[1] It corresponds to the shiny iridescent layer at the inner side of the carbonated shells (Figure 1a) of mollusks such as bivalves, gastropods, cephalopods, and monoplacophorans. This composite material is made of $CaCO_3$ mineral tablets in the form of aragonite (∼95 wt % of the whole shell) and an organic matrix (∼5 wt %) which is proposed to control nucleation and crystal growth as well as to define the specific microstructure and mineralogy of the shell layers.[2−4] The three-dimensional (3D) organization of the tablets varies from one species to another, forming a brick wall-like disposition for bivalves or a columnar structure in the case of gastropods.[5−8] In abalone shell, aragonite crystals form polygonal tablets of ∼5 to 10 μm in diameter and ∼0.5 to 1 μm in thickness.[9,10]

Two main organo−mineral interfaces are found in nacre. They are associated with the interlamellar and the intertabular organic fractions. The former is a 20−50 nm thick sheet located between lamellae made of tablets, whereas the latter is a thin membrane that laterally separates tablets within a single lamella. Both organic fractions are composed of different types of organic molecules: proteins, polysaccharides, and presumably lipids.[9,11−14] The polysaccharide moiety includes β-chitin, sulfatic, and acidic polysaccharides[5,14−18] while the proteinaceous component consists of two fractions described as insoluble and soluble in acidic solvents, the so-called silk and acidic proteins, respectively. Silk proteins, displaying similarities with arthropod silk, are the major protein fraction and are present in a hydrogel-like state located in-between β-chitin layers.[19] Acidic proteins are particularly rich in acidic amino acid[20] and are dispersed within the silk gel-like phase.[3,21]

In abalone nacre, aragonite tablets are stacked in a columnar arrangement where their centers are mainly aligned.[5,9,22] Once nacre is formed, the interlamellar and intertabular organic fractions are proposed to act as a cement joining the aragonite tablets. This layered organization offers a great example of homogeneity and gives to nacre its remarkable mechanical

Received: May 15, 2023
Revised: June 28, 2023
Published: July 24, 2023

properties in terms of strength and toughness.[11] As a result, nacre is 3000 times more fracture-resistant than pure aragonite crystals.[23,11]

Three main nacre growth mechanisms have been proposed:

(i) The heteroepitaxy mechanism[24] proposes that the mineral nucleation is driven by a direct atomic match with the organic layers of the shell matrix.[22,25] Further works proposed that acidic proteins adsorbed onto the chitin layer and localized at the center of the tablet surface would initiate the aragonite nucleation.[26,27] Single points of nucleation, rich in acidic proteins, would be aligned normal to the organic layers, orienting the nacre columnar arrangement.[26]

(ii) The homoepitaxy mechanism proposes that mineral growth occurs through mineral bridges across nanopores located within the organic layered matrix.[28] This mineral−mineral contact induces a crystallographic continuity between superimposed tablets in a nacre column where the *c*-axis is perpendicular to the organic interlamellar layer.[9,28] Alternatively, only central mineral bridges were observed at the center of the base of each tablet in the columnar arrangement in both gastropods and *Nautilus* cephalopods.[29,30] Nevertheless, TEM analysis of *Pinctada maxima*'s nacre revealed that some bridges have an organic nature.[31]

(iii) Olson et al. 2013 proposed that nacre formation could result from both mechanisms where the unique central large pore, allowing for the crystallographic continuity, would be surrounded by acidic organic molecules controlling the mineral nucleation.[32] After nucleation, the forming crystal grows in the *c*-direction perpendicular to the organic sheet until it reaches the next pre-positioned organic matrix layer.

Besides, the highly ordered nacreous structure was proposed to be a self-assembly process controlled by thermodynamics and kinetics of crystal growth in *Haliotis asinina* gastropod and other mollusks.[33]

At this point, and independently of the proposed growth mechanism, the tablet stops to grow in thickness and starts to extend parallel to the (longitudinal) organic matrix sheets.[26,34] Such lateral growth is described to occur within the space between the last two formed interlamellar membranes containing a confined gel-like phase rich in silk fibroins and acidic proteins.[13] It is proposed that during the lateral mineral expansion, some organic molecules are entrapped within individual crystallites inducing some anisotropic lattice distortions as observed in mollusk shells.[35] These protein inclusions might also be related to the carbon-rich voids identified within aragonite tablets in *Haliotis laevigata*[36] or the nano-inclusions rich in biomolecules found in *Perna canaliculus*[37] and *Pinctada fucata*.[38] The lateral growth then ends by contact inhibition with an adjacent tablet.

Once the nacre formation is achieved, aragonite tablets are not fully crystallized and a disordered mineral surface layer has been evidenced in *H. laevigata*,[39] *Haliotis tuberculata*,[40] and *Perna viridis*.[41] Moreover, in *Perna canaliculus*, solid-state NMR analysis evidenced a small fraction of disordered interfacial carbonates that were found to interact with biomolecules, bicarbonates, and water molecules.[42]

According to the above-mentioned observations and proposed mechanisms, the following organo−mineral interfaces can be thus potentially identified within the growing nacre (Figure 1b): (1) in the central zone of the tablets possibly identified as nucleation sites, (2) between the lateral mineral surfaces of the tablets and the silk gel during lateral growth, (3) between the lateral mineral surfaces of the tablets and the intertabular membrane once the lateral expansion of the tablets is achieved, (4) between the lamellae long surfaces and the interlamellar organic sheets, and (5) within the tablets, i.e., between the intra-crystalline organic inclusions and the mineral bulk.

Despite the diversity of the studies, the exact nature of these organo-mineral interfaces (i.e., molecular and ionic species

involved as well as chemical interaction) is not fully known. It is based on *in vitro* and *in vivo* models, it is reported that the mentioned above acidic proteins control crystal nucleation, polymorphism, morphology, and orientation of calcium carbonate crystallites;[3,20,21,43] their acidic nature favoring the interaction with the mineral fraction through calcium ion binding. Moreover, the presence of enzymes such as carbonic anhydrase catalyzes the formation of CO_3^{2-}.[44] Different post-translational modifications of proteins can occur such as glycosylation, sulfatation, and phosphorylation, which are crucial for their physiological functions.[26]

Here, we investigate the different organo−mineral interfaces in growing nacre thanks to high-resolution analyses of the European abalone *H. tuberculata*shell (Figure 1a), a key model to investigate the mechanisms of nacre formation.[10,45] We mainly focus on (*i*) the central region (region 1 in Figure 1b) and (*ii*) the lateral surfaces (region 2 in Figure 1b) of the tablets. Firstly, focused ion beam (FIB) milling coupled with field emission gun scanning electron microscopy (FEG-SEM) allowed for the precise selection and preparation of an ultrathin section within the columnar arrangement of growing nacre in *H. tuberculata*'s shell. Then, in addition to high-resolution TEM (HR-TEM), spatially and spectrally highly resolved spectromicroscopy techniques such as scanning transmission X-ray microscopy (STXM) and electron energy loss spectroscopy in a scanning transmission electron microscope (STEM-EELS) were used to gain local information on the nature of the organo−mineral interfaces and more precisely, to discriminate organic vs mineral carbons. In particular, we show that the central domain in aragonite tablets is of organic nature which appears to further extend within the interlamellar space co-existing with aragonite. This suggests that a hybrid bridge drives the resulting columnar arrangement strengthening previous observations in the literature.[7,26,28] Moreover, a second organic-rich region is identified at the lateral tablet surfaces as a disordered domain deficient in carbonates that is, however, surprisingly rich in calcium ions. The demonstration of predominant organic-rich domains at the nanoscale offers a better understanding of the processes involved in nacre formation.

2. EXPERIMENTAL SECTIONS

2.1. Material and Sample Preparation. One-year-old European abalone, *H. tuberculata*, specimens were obtained from *France Haliotis* farm (48°36′46N, 4°33′30W; Plouguerneau, France). After dissection, shells measuring ∼1 cm in length were washed with distilled water, dried and stored at room temperature until analysis.

2.2. Focused Ion Beam Milling. FIB milling was performed on the nacre layer of 1-year-old abalone shell using a Zeiss Neon40EsB CrossBeam instrument. A thin section measuring approximatively 100 nm in thickness was prepared.

3. METHODS

3.1. FEG-SEM. FEG-SEM observations were done using a Zeiss Ultra55 with an accelerating voltage of 3 kV.

3.2. HR-TEM. HR-TEM observation experiments were performed on a JEOL-2100F microscope equipped with a field emission gun operating at 200 kV, a and a scanning TEM (STEM) device, which allows Z-contrast imaging in the high-angle annular dark-field (HAADF) mode (STEM-HAADF). FFT image analyses were achieved using ImageJ software (https://imagej.nih.gov/).

3.3. STXM. STXM analyses were performed on the HERMES Beamline at the SOLEIL synchrotron light source.[46] The SOLEIL storage ring operated at 2.75 GeV and 430 mA stored current in the top-up mode. A plane grating monochromator with a 450 L/mm grating and 25 μm exit slit was used for carbon imaging and spectroscopy, providing a theoretical energy resolution better than 100 meV. Energy calibration was accomplished using the well-resolved 3p Rydberg peak at 294.96 eV of gaseous CO_2. A zone plate was used to focus the X-ray beam to a spot size of ∼50 nm. An image stack was collected by scanning the FIB section in $x-y$ direction (image stack) at energy increments of 0.12 eV for carbon, over the 280−320 eV energy range of interest. Counting time was 4 milliseconds per pixel and per energy step. Data were processed using the aXis2000 software. Maps were obtained by fitting the hyperspectral data with endmember spectra extracted from the dataset.[47]

3.4. STEM-HAADF and EELS Acquisitions. HAADF images and electron energy loss spectroscopy (EELS) data were obtained at 100 kV using a VG HB501 Scanning Transmission Electron Microscope (STEM) equipped with a cold field emission gun, a home modified Gatan spectrometer, and a homemade cryo-stage to minimize the beam radiation damage. EEL spectra were collected with an energy dispersion of 0.5 eV/channel in the energy range from 100 to 500 eV comprising the absorption edges of the elements of interest (carbon and calcium). Typical energy resolution was about 1 eV measured from the zero loss peak and the spatial resolution determined by the beam diameter was approximately 1 nm. EELS data were acquired in the spectrum-imaging mode[48] for which the focused beam is scanned over a region of interest and a whole spectrum is acquired at each position of the scan (see Supporting Information). A typical hyperspectral image contains about 10,000 spectra. The EELS energy scale was calibrated using the peak corresponding to 1s → π^* transitions in carbonate carbon at 290.3 eV and the main Ca $L_{2,3}$-edge peak at 349 eV.[49] Data were first processed to improve the signal-to-noise ratio using principal component analysis (PCA) under Hyperspy, an open-source software suite as a denoising method.[50]

4. RESULTS AND DISCUSSION

The growing edge of the inner nacreous layer in one-year-old *H. tuberculata* shell was first observed by FEG-SEM. The transition between the spherulitic (s), the immature nacre (n_i), and the mature nacre (n_m) regions is easily observed in (Figure 1c) and (Figure S1), respectively, as previously observed in adult and juvenile *H tuberculata*.[10,51] Mature (n_m) (Figure 1d) and immature (n_i) (Figure 1e) nacres are distinguished based on the observation of aragonite platelets that are either joined side by side or not, respectively. In contrast, the spherulitic region displays featureless aragonite crystals associated with a loose organic matrix (Figure 1f), whereas the immature nacre, at the edge of the spherulitic region, exhibits a dense organic network (Figure 1e) with individual columnar arrangements similar to Christmas trees. Although this could be induced upon dehydration, it possibly indicates a difference in organic density between spherulitic and nacre regions.

We then used FEG-SEM coupled with FIB (Figure 1g) to select and mill a section perpendicular to the intermediate region of growing aragonite tablets, i.e., between the immature and mature regions of the growing nacre layer (inset, Figure 1g). The surface of the selected area was first coated with a platinum strap (star, Figure 1g). Then, FIB milling was performed to dig into the sample on both sides of the Pt strap down to several micrometers in depth (Figure S2). As expected, the FIB section shows that, within the most superficial layer of nacre columnar arrangement, the tablets do not meet laterally (Figure 1h) while they densify down to the mature nacre (Figure S3). Finally, this columnar arrangement was thinned down to ∼100 nm for STXM and EELS investigations.

4.1. Longitudinal Growth of Aragonite Tablets in Columnar Arrangement. FEG-SEM observations of the resulting ion-milled thin section reveal a brighter zone in the center of each tablet and thus all along the columnar arrangement (yellow arrow in Figure 2) similarly to a vertical backbone oriented along the *c*-axis of aragonite tablets (Figure 2a).

Further TEM observations of the section show that this backbone is possibly discontinuous since less contrasted submicron domains are observed in the center of each tablet, all along their width (Figure 2b). STEM-HAADF observations confirm the presence of such domains having a lower average electron density (darker zones) compared to the bulk and which are referred as "globules" here after (Figure 2c). They are irregular in shape and size with the largest ones measuring about 200 nm. Observations at higher magnification (Figure 2d) also reveal the presence of nanometric "defects" (10−50 nm) that are widespread inside the tablets reminding organic inclusions formed in calcite *in vitro*.[52] In contrast to the central globules, these "nanodefects" are homogeneously dispersed within the mineral phase (zone 5 in Figure 1b). Such nanometer-sized "defects" or inclusions remind those found in the nacre layer of *H. laevigata*,[36] *P. canaliculus*,[37] and *P. fucata*[53] shown to contain biomacromolecules.

The central interlamellar region was further investigated at higher magnification by HR-TEM (Figure 3). Bridging structures are observed between the tablets in this area measuring about 100 nm in length and 10−50 nm in width (Figure 3a−c). They co-exist with crystalline mineral protuberances (white arrows, Figure 3b,d) that can be surrounded by an amorphous layer (white star, Figure 3b). In addition, Fast-Fourier Transform (FFT) performed on selected areas of an aragonite tablet (1 in Figure 3c) and along the bridging structures (2 and 4 in Figure 3c) reveal that these latter are not always non-crystalline. Indeed, we found that some of them are made of a mixture of an amorphous phase and aragonite (according to 3 in Figure 3c), which appears to be slightly misoriented along the [001] axis.[54] The fact that such hybrid bridges are only seen along the central region suggests that this zone is essential for setting the columnar arrangement in possibly linking the tablets together. This observation complements the crystalline mineral bridges reported before in other gastropods.[28,30]

To go deeper in the characterization of the central domain along the columnar arrangement, SEM-FEG observations were then performed on fractured nacre (Figure 3e,f). This allows the striping of the tablets unveiling either a protrusion or a defect (white arrows in Figure 3e) in the center of each tablet. These protrusions are about 400−500 nm in height, which is approximately the thickness of a tablet (Figure 3f). Consequently, they may consist of the globules and/or the amorphous bridges seen by HR-TEM.

This observation reminds that of the central organic-rich core described in other nacreous shells.[29,55−57] The common features with these previous works are (*i*) the organic-based nature of the material, (*ii*) the position at the center of the aragonite tablets, and (*iii*) the size range of the inclusions. However, it is difficult to conclude whether they are indeed identical since besides the different nature of the biological samples, their preparations and direction of observations are also not the same. From a mechanistic aspect, we do not have criteria to discard any of the proposed functions and can only speculate that their implications may be related to the formation of the soluble/insoluble organic and/or the mineral matrices. This observation may also be related to the identified carboxylated and sulfated proteins located right at the center of aragonite tablets and the surface of the interlamellar membrane, that are assigned to mineral nucleation sites.[26]

Therefore, in order to identify the chemical nature (organic and/or mineral) of the observed globular inclusions in the columnar arrangement, we further investigated the FIB thin section using scanning transmission X-ray microscopy (STXM). This spectromicroscopy technique provides images with a spatial resolution of about 50 nm and X-ray absorption near edge structure (XANES) spectra at the same spatial scale. XANES spectra were acquired at the carbon K-edge (280−320

eV), providing information about the speciation of carbon. In particular, inorganic (i.e., carbonates) vs organic carbon could be distinguished on this basis.[47] The investigated region of the FIB section was chosen in order to frame the central defects zone, the immature tablets and the organic layers (Figure 4a). Two different XANES spectra are detected in the hyperspectral data obtained on this area and explained most of the spectral variability (Figure 4b,c). The XANES spectrum (blue spectrum in Figure 4c) associated with the nacre tablets displays a narrow peak at 290.3 eV corresponding to 1s → π^* electronic transitions in carbonate CO_3^{2-}, as well as broader peaks at 296, 300, and 301.5 eV, corresponding to 1s → σ^* electronic transitions in carbonate CO_3^{2-} all consistent with almost pure aragonite.[58,59]

The second XANES spectrum (in red in Figure 4c) is measured prevalently around the nacre tablets. It corresponds to areas containing some carbonates but also a significant amount of organic material. Indeed, this XANES spectrum contains the peaks attributed to aragonite but additionally showed several other peaks at lower energies: in particular at 285.1, 286.7 eV and a broad peak between 288.2 and 288.6 eV that were interpreted as 1s → π^* electronic transition in aromatic, ketone and a mixture of amide and carboxylic acid carbon functional groups, respectively.[60] This spectrum is consistent with the presence of acidic proteins and possibly polysaccharide-rich organic assemblage surrounding aragonite tablets. However, it can be noted that the spectrum is significantly different from that of chitin, which shows prominent peaks at 288.4 and 289.4 eV at the C K-edge.[61] This might be explained by either the minor contribution of chitin to this organic assemblage and/or artifactual damages induced by FIB milling, which may have significantly altered the XANES spectrum of chitin. Supporting the latter hypothesis, we note that several previous studies have measured XANES spectra of FIB-milled bacterial cells, which were significantly different from the C K-edge XANES spectrum of a non-FIB-milled bacterium (e.g., compare Carlut et al. 2010[62] and Benzerara et al. 2004[63]). Unexpectedly, the XANES spectrum of the FIB-milled bacterium looks similar to the spectrum measured in the present study. While some studies have shown that FIB milling was preserving carbon functional groups of organic polymers such as Araldite,[64] the present observation suggests that it may not be the case for other polymers.

More importantly, we also evidence organic-rich regions in the central part of the nacre tablets suggesting that the globules observed by HR-TEM contain indeed organics. In addition, we note that this central zone within the tablets is not purely organic because an aragonite signal (peak at 290.3 eV in Figure 4e) is detected as well, suggesting a local association of the mineral and the organic phases. Interestingly, such organic structure could act as a glue for such high stiffness/strength mineral tablets resulting in optimized mechanical properties as reported e.g., for amorphous calcium ions-organic materials in bone.[65]

A closer analysis of the blue spectra measured in the tablets (Figure 4d) shows that the 285.1, 286.7, and 288.4 eV peaks corresponding to organic matter are also present although to a lower extent. This indicates that the interior of the tablets may also contain some organics in addition to aragonite. This signal might result from intra-crystalline proteins, which are trapped during the mineral tablet growth, and seems to correspond to the nanometer-sized defects shown in Figure 2d. Figure 4b highlights in addition that the lateral sides of immature tablets are also surrounded by an organic-rich layer investigated in details in the next part of our study.

4.2. Lateral Growth of Aragonite Tablets. HR-TEM observations were also performed on several lateral growing regions of aragonite tablets (zones 1, 2, and 3 in Figure 5a). In such growing zones, the tablets are not in contact laterally and two kinds of non-crystalline domains are always observed at the edge of the tablets surrounding the crystalline aragonitic core (Figure 5b–d). The inner one of 5 nm in average is in close contact with the crystalline aragonite core (denoted with "°" in Figure 5a) while the outer one covers the former and is quite homogeneous in size with a thickness varying between 15 and 20 nm ("*" in Figure 5a). The outer domain is therefore thicker than the inner one and is probably of organic nature. This latter might result from a shrinkage of the hydrated gel-like protein phase filling the space between two interlamellar sheets as described for *Atrina rigida* and *Pinctada margaritifera* in cryo-mode.[66] In contrast, the thinner domain appears to be the one previously described as intermediate amorphous mineral layer (~5 nm for *H. laevigata*[39] and *tuberculata*).[40] We note that the pyramidal nano-growths described by Yao et al.[67] along the vertical face of the platelets are mostly observed (zone 1 versus3) and found both on the surface and inside the crystalline core (Figure S4). Such differences may be explained by the fact that (*i*) the orientation of the section cut may favor their appearance and (*ii*) the degree of maturation is not the same since the work of Yao et al. the platelets are in contact and consequently more mature.

To investigate the chemical composition of the nano organo–mineral interfaces of the lateral growing regions, zone 1 (Figure 5b–g) and 4–5 (Figures S5 and S6, respectively) were analyzed by EEL spectroscopy. A complete EEL spectrum was recorded at each position over the scanned area with a spatial resolution of ~1 nm. While those spectra are directly comparable with XANES spectra obtained by STXM, they allowed mapping the spectral variations observed by STXM with a finer spatial resolution as shown previously.[68] The EELS spectra at the C K- and Ca $L_{2,3}$-edges measured at four different positions on the lateral edge of an aragonite tablet in zone 1 (Figure 5a) are shown in Figure 5b. The positions A and B are located at the lateral surface, whereas positions C and D are located *circa* 20 nm away, i.e., toward the inner part of the tablet (Figure 5c).

At the carbon K-edge, we observe two different patterns according to the probe position. For positions C and D, the spectrum is dominated by the presence of a narrow peak at 290.3 eV (peak 2 in Figure 5b) and a broad peak around 301 eV. These signatures are characteristic of 1s → π^* and 1s → σ^* transitions in carbonate functional groups as observed for the aragonite reference sample showed in Figure 5b (black curve). Consistently, they are in excellent agreement with XANES data presented in Figure 4. For positions A and B (surface), the spectra are characterized by the presence of a narrow peak at ~287 eV (peak 1 in Figure 5b) and a broad peak centered around 295 eV. These two peaks are characteristic of organic compounds such as proteins in particular (Figure S5). It has to be noticed that organic peak position is shifted to lower energy

in EELS compared to XANES due to beam-induced damage. On the basis of EELS data, we thus evidence that an organic fraction is dominant in the outer positions A and B, whereas in the inner positions C and D, inorganic carbonates are dominant.

The spatial distributions of carbonate and organic species were further determined by fitting the carbon peaks (see Text S5). The two corresponding maps (carbonate and organic compounds) are depicted in Figure 5e,f. In addition, a false-color composite image is displayed in Figure 5g. We observe that organic carbons are principally located in the outer region of the amorphous domain observed by HR-TEM, region that is deficient in carbonate compared to aragonite tablet. The colored map highlights the non-homogeneous distribution of these species: the organic fraction forms a regular outer domain of about 20 nm in thickness (in accordance with HR-TEM data).

When we move inwards the tablet, the thickness of the aragonite tablet increases and the EELS spectra get distorted. At larger thicknesses, the EELS signals disappear and it is no longer possible to detect the presence of the different species. The limit at which the spectra are too distorted to obtain reliable maps is indicated by a white line on the color maps (Figure 5g). Consequently, the organic-rich inclusions in the central area of the aragonite tables could not be investigated by EELS here.

Two peaks at ∼349 and ∼352 eV corresponding to the Ca-L_3- and L_2-edges, respectively, are observed for each position (Figure 5b). The elemental maps corresponding to calcium and carbonate distribution in the amorphous layer around the aragonite tablets were obtained from EELS data by integrating the intensity of the Ca-$L_{2,3}$ edge after background subtraction. The resulting map reveals that calcium (Figure 5g) is present in the whole investigated areas, both in the carbonate-rich and the organic-rich regions. This suggests the presence of three types of calcium ions that are: (*i*) associated with carbonates as a crystalline $CaCO_3$ phase in the inner region of the tablet, (*ii*) associated with organic components at the edge, and (*iii*) to a lesser extent with carbonates possibly in an amorphous $CaCO_3$ phase. The presence of calcium in this outer layer suggests the involvement of calcium-binding acidic proteins to control the lateral growth of aragonite tablets. The combination of these observations leads to the conclusion that the lateral surface layer of growing aragonite tablets is indeed composed of two domains: one outer domain of about 20 nm mostly composed of organic matter rich in calcium and deficient in carbonate that covers the second domain composed of amorphous $CaCO_3$ (* and ° seen through HR-TEM in Figure 5) ultimately surrounding the inner crystalline aragonite. We note that Mg ions are commonly described to stabilize ACC phases *in vivo*.[69,70] However, Mg was not detected by EDX (Figure S7).

These results seem to be generalized to the other regions as seen from the investigation of zones 4 and 5 from Figure 5a. In zone 4 (Figure S6), adjacent growing tablets are separated by ∼10 to 20 nm and an organic-rich surface domain of ∼10 nm is evidenced at the edge of each tablet. Similar to zone 1, it is depleted in carbonates (see position A in Figure S6), whereas calcium is still strongly detected. Finally, zone 5 (Figure S8), which is in the longitudinal growth direction but notably away from the central core, is particularly interesting because it displays a bridge between two tablets. This bridge is mostly depleted in carbonates as well (see C−K edge spectra at points A, B and C) and seems to be mainly composed of organics together with calcium ions.

As a conclusion from the EELS analysis, we evidenced that the lateral outer domain of growing aragonite tablets in nacre is not purely mineral but is mainly organic. This organic membrane was also described previously.[71] Interestingly, we evidence the presence of two types of calcium ions in the whole investigated growing areas: (*i*) within the $CaCO_3$ phase and (*ii*) within the organic layer. This strongly suggests the involvement of calcium-binding acidic proteins that might concentrate locally calcium ions during the growing process of mineral tablets. This calcium might react with carbonates in a second step to form calcium carbonate. It is coherent with recent results that reveal calcium combined with organic without carbonate during the first stages of biomineralization in *H. tuberculata*.[72]

It would be of high interest to perform similar investigations on other elements and especially on phosphorus. Indeed, it is known that phosphorylation is one of the most widespread post-translational modifications occurring in mineralizing proteins.[73,74] In invertebrates, phosphorylated shell matrix is more effective in inhibiting crystal growth than dephosphorylated matrix.[75] It is also known that phosphorylation of proteins can affect their interaction with calcium and possibly induce occlusion within crystals.[76] Finally, the co-occurrence of inorganic phosphate with calcium and carbonate throughout the early stages of formation of the European abalone shell was recently reported;[72] its presence in growing domains would extend its implication in aragonite formation.

5. CONCLUSION

In this work, we used a combination of high-resolution techniques to characterize chemically and structurally immature nacre of *H. tuberculata* shells. A thin section of a stack of more than 20 growing aragonite tablets was carefully prepared by FIB. We paid a particular attention to two regions: (*i*) the longitudinal axis of the columnar arrangement and (*ii*) the lateral surface of the aragonite tablets.

In case (*i*), we evidence by HR-TEM observations and STXM analysis large disordered organic-rich inclusions localized in the center of the tablets, and thus being aligned along the *c*-axis direction of aragonite i.e., the columnar arrangement. These organic globular inclusions extend from one tablet to another through hybrid bridges composed of an aragonite core surrounded by organics. In addition, the aragonitic cores have the same *c*-axis orientation than that of the tablets. We note that the tablets appear to be slightly misoriented along the [001] axis. These organic globules might act as an organic backbone which could be essential for the setting of the longitudinal arrangement of the stacked tablets strengthening similar assumptions for other species.

In case (*ii*), we evidence by HR-TEM observations and EELS analysis a 20 nm thick disordered domain at the surface of immature aragonite tablet thus in contact with the amorphous $CaCO_3$ mineral layer. This outer domain is mainly composed of an organic fraction and is deficient in carbonates. However, calcium is still present within this domain suggesting the presence of calcium-binding acidic proteins that control the lateral growth of aragonite. The organic domain could result from the interlamellar silk fibroin gel rich in acidic soluble proteins in which the tablets grow.

Overall, this work demonstrates the potential of STXM and EELS for high-resolution chemical analysis of complex nano

organo−mineral interfaces in nacre and in particular for the discrimination of organic *vs* inorganic carbon.

■ ASSOCIATED CONTENT

Supporting Information

The Supporting Information is available free of charge at https://pubs.acs.org/doi/10.1021/acs.chemmater.3c01169.

Additional SEM FEG and HR-TEM observations, EEL spectra at the C−K edge and the Ca-L_{23} edge, and EDX analysis of growing aragonite tablets (PDF)

■ AUTHOR INFORMATION

Corresponding Authors

Stéphanie Auzoux-Bordenave − *Laboratoire de Biologie des Organismes et Ecosystèmes Aquatiques" (BOREA), Muséum National D'histoire Naturelle/CNRS/IRD/Sorbonne Université/UCN/UA/Station Marine de Concarneau, 29900 Concarneau, France*; Email: stephanie.auzoux-bordenave@mnhn.fr

Thierry Azaïs − *Sorbonne Université, CNRS, Collège de France, Laboratoire de Chimie de la Matière Condensée de Paris (LCMCP), F-75005 Paris, France;* orcid.org/0000-0002-9031-872X; Email: thierry.azais@sorbonne-universite.fr

Nadine Nassif − *Sorbonne Université, CNRS, Collège de France, Laboratoire de Chimie de la Matière Condensée de Paris (LCMCP), F-75005 Paris, France;* orcid.org/0000-0002-4094-4909; Email: nadine.nassif@sorbonne-universite.fr

Authors

Widad Ajili − *Sorbonne Université, CNRS, Collège de France, Laboratoire de Chimie de la Matière Condensée de Paris (LCMCP), F-75005 Paris, France; Laboratoire de Biologie des Organismes et Ecosystèmes Aquatiques" (BOREA), Muséum National D'histoire Naturelle/CNRS/IRD/Sorbonne Université/UCN/UA/Station Marine de Concarneau, 29900 Concarneau, France*

Marta de Frutos − *Laboratoire de Physique des Solides, Université Paris-Saclay, CNRS UMR 8502, F-91405 Orsay, France;* orcid.org/0000-0002-9053-1723

Imène Estève − *Sorbonne Université, Muséum National D'Histoire Naturelle, UMR CNRS 7590, IRD, Institut de Minéralogie, de Physique des Matériaux et de Cosmochimie, IMPMC, 75005 Paris, France*

Marie Albéric − *Sorbonne Université, CNRS, Collège de France, Laboratoire de Chimie de la Matière Condensée de Paris (LCMCP), F-75005 Paris, France;* orcid.org/0000-0002-5322-9904

Nicolas Menguy − *Sorbonne Université, Muséum National D'Histoire Naturelle, UMR CNRS 7590, IRD, Institut de Minéralogie, de Physique des Matériaux et de Cosmochimie, IMPMC, 75005 Paris, France*

Karim Benzerara − *Sorbonne Université, Muséum National D'Histoire Naturelle, UMR CNRS 7590, IRD, Institut de Minéralogie, de Physique des Matériaux et de Cosmochimie, IMPMC, 75005 Paris, France*

Antonio Checa − *Department of Stratigraphy and Paleontology, University of Granada, 18071 Granada, Spain;* orcid.org/0000-0001-7873-7545

Complete contact information is available at: https://pubs.acs.org/10.1021/acs.chemmater.3c01169

Notes

The authors declare no competing financial interest.

■ ACKNOWLEDGMENTS

The authors thank Sylvain Huchette from the France Haliotis farm (Plouguerneau, France) who provided abalone for the experiments. This work was supported by French state funds managed by the ANR within the Investissements d'Avenir programme under reference ANR-11-IDEX-0004-02, and more specifically within the framework of the Cluster of Excellence MATISSE led by Sorbonne Université. This work was also supported by the Regional Council of Brittany (France), the programme Emergence (Sorbonne Université) funded by the Ministère délégué à l'Enseignement Supérieur et à la Recherche (Paris, France) and the European Union's Horizon 2020 Research and Innovation Programme under grant agreement no 823717. FIB and SEM facility of IMPMC was supported by Région Ile de France Grant SESAME 2006 NOI-07-593/R, Institut National des Sciences de l'Univers (INSU)−CNRS, Institut de physique—CNRS, Sorbonne Université, and the French National Research Agency (ANR) grant ANR-07-BLAN-0124-01.

■ REFERENCES

(1) Carpenter, W. B. On the microscopic structure of shells. *British Association for the Advancement of Science: Part II*; the University of Michigan, 1844; Vol. *17*(93134), p 4.

(2) Addadi, L.; Weiner, S. Interactions between acidic proteins and crystals: stereochemical requirements in biomineralization. *Proc. Natl. Acad. Sci. U.S.A.* **1985**, *82*, 4110−4114.

(3) Falini, G.; Albeck, S.; Weiner, S.; Addadi, L. Control of Aragonite or Calcite Polymorphism by Mollusk Shell Macromolecules. *Science* **1996**, *271*, 67−69.

(4) Marin, F.; Luquet, G.; Marie, B.; Medakovic, D. Molluscan Shell Proteins: Primary Structure, Origin, and Evolution. In *Current Topics in Developmental Biology*; Schatten, G. P., Ed.; Elsevier Academic Press Inc: San Diego, 2008; Vol. *80*, pp 209−276.

(5) Wise, S. W. Microarchitecture and Deposition of Gastropod Nacre. *Science* **1970**, *167*, 1486−1488.

(6) Nakahara, H. Nacre formation in bivalve and gastropod molluscs. *Mechanisms and Phylogeny of Mineralization in Biological Systems*; Suga, S., Nakahara, H., Eds.; Springer-Verlag: Berlin, 1991; Chapter 4.2, pp 343−350.

(7) Checa, A. G.; Ramírez-Rico, J.; González-Segura, A.; Sánchez-Navas, A. Nacre and false nacre (foliated aragonite) in extant monoplacophorans (= Tryblidiida: Mollusca). *Naturwissenschaften* **2009**, *96*, 111−122.

(8) Dauphin, Y.; Luquet, G.; Salome, M.; Bellot-Gurlet, L.; Cuif, J. P. Structure and composition of Unio pictorum shell: arguments for the diversity of the nacroprismatic arrangement in molluscs. *J. Microsc.* **2018**, *270*, 156−169.

(9) Heinemann, F.; Launspach, M.; Gries, K.; Fritz, M. Gastropod Nacre: Structure, Properties and Growth — Biological, Chemical and Physical Basics. *Biophys. Chem.* **2011**, *153*, 126−153.

(10) Auzoux-Bordenave, S.; Brahmi, C.; Badou, A.; de Rafélis, M.; Huchette, S. Shell Growth, Microstructure and Composition over the Development Cycle of the European Abalone Haliotis tuberculata. *Mar. Biol.* **2015**, *162*, 687−697.

(11) Jackson, A. P.; Vincent, J. F. V.; Turner, R. M. The Mechanical Design of Nacre. *Proc. R. Soc. London, Ser. B* **1988**, *234*, 415−440.

(12) Watabe, N.; Wilbur, K. Influence of the Organic Matrix on Crystal Type in Molluscs. *Nature* **1960**, *188*, 334.

(13) Bevelander, G.; Nakahara, H. An electron microscope study of the formation of the nacreous layer in the shell of certain bivalve molluscs. *Calcif. Tissue Res.* **1969**, *3*, 84−92.

(14) Weiner, S.; Traub, W. X-ray diffraction study of the insoluble organic matrix of mollusk shells. *FEBS Lett.* **1980**, *111*, 311−316.
(15) Crenshaw, M. A. The soluble matrix from Mercenaria mercenaria shell. *Biomineralization* **1972**, *6*, 6−11.
(16) Weiner, S.; Talmon, Y.; Traub, W. Electron diffraction of mollusc shell organic matrices and their relationship to the mineral phase. *Int. J. Biol. Macromol.* **1983**, *5*, 325−328.
(17) Kono, H. Two-dimensional magic angle spinning NMR investigation of naturally occurring chitins: precise ^{1}H and ^{13}C resonance assignment of α-and β-chitin. *Biopolymers* **2004**, *75*, 255−263.
(18) Marie, B.; Luquet, G.; Pais De Barros, J. P.; Guichard, N.; Morel, S.; Alcaraz, G.; Bollache, L.; Marin, F. The shell matrix of the unionid freshwater mussel Unio pictorum (Paleoheterodonta, Unionoida): Involvement of acidic polysaccharides from glycoproteins in nacre mineralization. *FEBS J.* **2007**, *274*, 2933−2945.
(19) Addadi, L.; Joester, D.; Nudelman, F.; Weiner, S. Mollusk Shell Formation: A Source of New Concepts for Understanding Biomineralization Processes. *Chem.—Eur. J.* **2006**, *12*, 980−987.
(20) Belcher, A. M.; Wu, X. H.; Christensen, R. J.; Hansma, P. K.; Stucky, G. D.; Morse, D. E. Control of Crystal Phase Switching and Orientation by Soluble Mollusc-Shell Proteins. *Nature* **1996**, *381*, 56−58.
(21) Weiner, S.; Dove, P. M. An Overview of Biomineralization Processes and the Problem of the Vital Effect. *Rev. Mineral. Geochem.* **2003**, *54*, 1−29.
(22) Lin, A.; Meyers, M. A. Growth and structure in abalone shell. *Mater. Sci. Eng., A* **2005**, *390*, 27−41.
(23) Currey, J. D. Mechanical properties of mother of pearl in tension. *Proc. R. Soc. London, Ser. B* **1977**, *196*, 443−463.
(24) Weiner, S.; Traub, W. Macromolecules in Mollusc Shells and Their Functions in Biomineralization. *Philos. Trans. R. Soc., B* **1984**, *304*, 425−434.
(25) Furuhashi, T.; Schwarzinger, C.; Miksik, I.; Smrz, M.; Beran, A. Molluscan shell evolution with review of shell calcification hypothesis. *Comp. Biochem. Physiol., Part B: Biochem. Mol. Biol.* **2009**, *154*, 351−371.
(26) Nudelman, F.; Gotliv, B. A.; Addadi, L.; Weiner, S. Mollusk shell formation: mapping the distribution of organic matrix components underlying a single aragonitic tablet in nacre. *J. Struct. Biol.* **2006**, *153*, 176−187.
(27) Bezares, J.; Asaro, R. J.; Hawley, M. Macromolecular structure of the organic framework of nacre in Haliotis rufescens: implications for growth and mechanical behavior. *J. Struct. Biol.* **2008**, *163*, 61−75.
(28) Schäffer, T. E.; Ionescu-Zanetti, C.; Proksch, R.; Fritz, M.; Walters, D. A.; Almqvist, N.; Zaremba, C. M.; Belcher, A. M.; Smith, B. L.; Stucky, G. D.; Morse, D. E.; Hansma, P. K. Does abalone nacre form by heteroepitaxial nucleation or by growth through mineral bridges? *Chem. Mater.* **1997**, *9*, 1731−1740.
(29) Checa, A. G.; Cartwright, J. H.; Willinger, M. G. The key role of the surface membrane in why gastropod nacre grows in towers. *Proc. Natl. Acad. Sci. U.S.A.* **2009**, *106*, 38−43.
(30) Checa, A. G.; Cartwright, J. H. E.; Willinger, M.-G. Mineral Bridges in Nacre. *J. Struct. Biol.* **2011**, *176*, 330−339.
(31) Rousseau, M.; Lopez, E.; Stempflé, P.; Brendlé, M.; Franke, L.; Guette, A.; Naslain, R.; Bourrat, X. Multiscale Structure of Sheet Nacre. *Biomaterials* **2005**, *26*, 6254−6262.
(32) Olson, I. C.; Blonsky, A. Z.; Tamura, N.; Kunz, M.; Pokroy, B.; Romao, C. P.; White, M. A.; Gilbert, P. U. P. A. Crystal nucleation and near-epitaxial growth in nacre. *J. Struct. Biol.* **2013**, *184*, 454−463.
(33) Schoeppler, V.; Lemanis, R.; Reich, E.; Pusztai, T.; Gránásy, L.; Zlotnikov, I. Crystal growth kinetics as an architectural constraint on the evolution of molluscan shells. *Proc. Natl. Acad. Sci. U.S.A.* **2019**, *116*, 20388−20397.
(34) Fritz, M.; Belcher, A. M.; Radmacher, M.; Walters, D. A.; Hansma, P. K.; Stucky, G. D.; Morse, D. E.; Mann, S. Flat Pearls from Biofabrication of Organized Composites on Inorganic Substrates. *Nature* **1994**, *371*, 49−51.
(35) Pokroy, B.; Fieramosca, J. S.; Von Dreele, R. B.; Fitch, A. N.; Caspi, E. N.; Zolotoyabko, E. Atomic Structure of Biogenic Aragonite. *Chem. Mater.* **2007**, *19*, 3244−3251.
(36) Gries, K.; Kröger, R.; Kübel, C.; Schowalter, M.; Fritz, M.; Rosenauer, A. Correlation of the orientation of stacked aragonite platelets in nacre and their connection via mineral bridges. *Ultramicroscopy* **2009**, *109*, 230−236.
(37) Younis, S.; Kauffmann, Y.; Bloch, L.; Zolotoyabko, E. Inhomogeneity of nacre lamellae on the nanometer length scale. *Cryst. Growth Des.* **2012**, *12*, 4574−4579.
(38) Suzuki, M.; Okumura, T.; Nagasawa, H.; Kogure, T. Localization of intracrystalline organic macromolecules in mollusk shells. *J. Cryst. Growth* **2011**, *337*, 24−29.
(39) Nassif, N.; Pinna, N.; Gehrke, N.; Antonietti, M.; Jäger, C.; Cölfen, H. Amorphous Layer around Aragonite Platelets in Nacre. *Proc. Natl. Acad. Sci. U.S.A.* **2005**, *102*, 12653−12655.
(40) Ajili, W.; Laurent, G. P.; Menguy, N.; Gansmuller, A.; Huchette, S.; Auzoux-Bordenave, S.; Nassif, N.; Azaïs, T. Chemical Heterogeneities within the Disordered Mineral domains of Aragonite Platelets in nacre from the European Abalone Haliotis tuberculata. *J. Phys. Chem. C* **2020**, *124*, 14118−14130.
(41) Zhang, G.; Xu, J. From Colloidal Nanoparticles to a Single Crystal: New Insights into the Formation of Nacre's Aragonite Tablets. *J. Struct. Biol.* **2013**, *182*, 36−43.
(42) Ben Shir, I.; Kababya, S.; Katz, I.; Pokroy, B.; Schmidt, A. Exposed and Buried Biomineral Interfaces in the Aragonitic Shell of Perna Canaliculus Revealed by Solid-State NMR. *Chem. Mater.* **2013**, *25*, 4595−4602.
(43) Fang, D.; Xu, G.; Hu, Y.; Pan, C.; Xie, L.; Zhang, R. Identification of genes directly involved in shell formation and their functions in pearl oyster, Pinctada fucata. *PLoS One* **2011**, *6*, No. e21860.
(44) Marin, F.; Luquet, G. Molluscan Shell Proteins. *Comptes Rendus Palevol* **2004**, *3*, 469−492.
(45) Auzoux-Bordenave, S.; Badou, A.; Gaume, B.; Berland, S.; Helléouet, M.-N.; Milet, C.; Huchette, S. Ultrastructure, Chemistry and Mineralogy of the Growing Shell of the European Abalone Haliotis tuberculata. *J. Struct. Biol.* **2010**, *171*, 277−290.
(46) Belkhou, R.; Stanescu, S.; Swaraj, S.; Besson, A.; Ledoux, M.; Hajlaoui, M.; Dalle, D. HERMES: a soft X-ray beamline dedicated to X-ray microscopy. *J. Synchrotron Radiat.* **2015**, *22*, 968−979.
(47) Cosmidis, J.; Benzerara, K. Soft x-ray scanning transmission spectromicroscopy. In *Biomineralization Source book: Characterization of Biominerals and Biomimetic Materials*; Di Masi, E., Gower, L. B., Eds.; CRC Press: New York, NY, 2014, pp 115−133.
(48) Jeanguillaume, C.; Colliex, C.; Ballongue, P.; Teneé, M. New STEM multisignal imaging modes, made accessible through the evaluation of detection efficiencies. *Ultramicroscopy* **1992**, *45*, 205−217.
(49) Cosmidis, J.; Benzerara, K.; Nassif, N.; Tyliszczak, T.; Bourdelle, F. Characterization of Ca-phosphate biological materials by scanning transmission X-ray microscopy (STXM) at the Ca L2, 3-P L2, 3-and C K-edges. *Acta Biomater.* **2015**, *12*, 260−269.
(50) De La Peña, F.; Prestat, E.; Fauske, V. T.; Burdet, P.; Furnival, T.; Jokubauskas, P.; Nord, M.; Ostasevicius, T.; Lähnemann, J.; MacArthur, K. E.; Johnstone, D. N.; Sarahan, M.; Taillon, J.; Aarholt, T.; Pquinn-Dls; Migunov, V.; Eljarrat, A.; Caron, J.; Mazzucco, S.; Martineau, B.; Somnath, S.; Poon, T.; Slater, T.; Francis, C.; Actions-User; Walls, M.; Cautaerts, N.; Tappy, N.; Winkler, F.; Donval, G. *Hyperspy/Hyperspy: Release v1.6.2*, 2021. https://zenodo.org/record/4683076.
(51) Badou, A.; Pont, S.; Auzoux-Bordenave, S.; Lebreton, M.; Bardeau, J. F. New insight on spatial localization and microstructures of calcite-aragonite interfaces in adult shell of Haliotis tuberculata: Investigations of wild and farmed abalones by FTIR and Raman mapping. *J. Struct. Biol.* **2022**, *214*, 107854.
(52) Page, M.; Nassif, N.; Börner, H. G.; Antonietti, M.; Cölfen, H. Mesoporous Calcite by Polymer Templating. *Cryst. Growth Des.* **2008**, *8*, 1792−1794.

(53) Suzuki, M.; Okumura, T.; Nagasawa, H.; Kogure, T. Localization of intracrystalline organic macromolecules in mollusk shells. *J. Cryst. Growth* **2011**, *337*, 24−29.
(54) Gilbert, P. U. P. A.; Metzler, R. A.; Zhou, D.; Scholl, A.; Doran, A.; Young, A.; Kunz, M.; Tamura, N.; Coppersmith, S. N. Gradual ordering in red abalone nacre. *J. Am. Chem. Soc.* **2008**, *130*, 17519−17527.
(55) Mutvei, H. The nacreous layer in molluscan shells. *The Mechanisms of Biomineralization in the Animals and Plants*; Omori, M., Watabe, N., Eds.; Tokay Univ Press: Tokyo, 1980; pp 49−56.
(56) Mutvei, H. Ultrastructural evolution of molluscan nacre. *Biomineralization and Biological Metal Accumulation: Biological and Geological Perspectives Papers presented at the Fourth International Symposium on Biomineralization, Renesse, The Netherlands, June 2−5, 1982*; Springer Netherlands, 1983; pp 267−271.
(57) Nakahara, H. Calcification of gastropod nacre. *Biomineralization and Biological Metal Accumulation: Biological and Geological Perspectives Papers presented at the Fourth International Symposium on Biomineralization, Renesse, The Netherlands, June 2−5, 1982*; Springer Netherlands, 1983; pp 225−230.
(58) Zhou, D.; Metzler, R. A.; Tyliszczak, T.; Guo, J.; Abrecht, M.; Coppersmith, S. N.; Gilbert, P. U. P. A. Assignment of polarization-dependent peaks in carbon K-edge spectra from biogenic and geologic aragonite. *J. Phys. Chem. B* **2008**, *112*, 13128−13135.
(59) Benzerara, K.; Meibom, A.; Gautier, Q.; Kaźmierczak, J.; Stolarski, J.; Menguy, N.; Brown, G. E., Jr. Nanotextures of aragonite in stromatolites from the quasi-marine Satonda crater lake, Indonesia. *Geol. Soc. Spec. Publ.* **2010**, *336*, 211−224.
(60) Cosmidis, J.; Benzerara, K.; Menguy, N.; Arning, E. Microscopy evidence of bacterial microfossils in phosphorite crusts of the Peruvian shelf: Implications for phosphogenesis mechanisms. *Chem. Geol.* **2013**, *359*, 10−22.
(61) Solomon, D.; Lehmann, J.; Kinyangi, J.; Liang, B.; Heymann, K.; Dathe, L.; Hanley, K.; Wirick, S.; Jacobsen, C. Carbon (1s) NEXAFS Spectroscopy of Biogeochemically Relevant Reference Organic Compounds. *Soil Sci. Soc. Am. J.* **2009**, *73*, 1817−1830.
(62) Carlut, J.; Benzerara, K.; Horen, H.; Menguy, N.; Janots, D.; Findling, N.; Addad, A.; Machouk, I. Microscopy study of biologically mediated alteration of natural mid-oceanic ridge basalts and magnetic implications. *J. Geophys. Res.* **2010**, *115*, G00G11.
(63) Benzerara, K.; Yoon, T. H.; Tyliszczak, T.; Constantz, B.; Spormann, A. M.; Brown, G. E., Jr. Scanning transmission X-ray microscopy study of microbial calcification. *Geobiology* **2004**, *2*, 249−259.
(64) Bernard, S.; Benzerara, K.; Beyssac, O.; Brown, G. E., Jr; Stamm, L. G.; Duringer, P. Ultrastructural and chemical study of modern and fossil sporoderms by Scanning Transmission X-ray Microscopy (STXM). *Rev. Palaeobot. Palynol.* **2009**, *156*, 248−261.
(65) Fantner, G. E.; Hassenkam, T.; Kindt, J. H.; Weaver, J. C.; Birkedal, H.; Pechenik, L.; Cutroni, J. A.; Cidade, G. A. G.; Stucky, G. D.; Morse, D. E.; Hansma, P. K. Sacrificial bonds and hidden length dissipate energy as mineralized fibrils separate during bone fracture. *Nat. Mater.* **2005**, *4*, 612−616.
(66) Nudelman, F.; Shimoni, E.; Klein, E.; Rousseau, M.; Bourrat, X.; Lopez, E.; Addadi, L.; Weiner, S. Forming nacreous layer of the shells of the bivalves Atrina rigida and Pinctada margaritifera: an environmental-and cryo-scanning electron microscopy study. *J. Struct. Biol.* **2008**, *162*, 290−300.
(67) Yao, N.; Epstein, A. K.; Liu, W. W.; Sauer, F.; Yang, N. Organic−inorganic interfaces and spiral growth in nacre. *J. R. Soc. Interface* **2009**, *6*, 367−376.
(68) Benzerara, K.; Menguy, N.; Guyot, F.; Vanni, C.; Gillet, P. TEM study of a silicate-carbonate-microbe interface prepared by focused ion beam milling. *Geochim. Cosmochim. Acta* **2005**, *69*, 1413−1422.
(69) Von Euw, S.; Zhang, Q.; Manichev, V.; Murali, N.; Gross, J.; Feldman, L. C.; Gustafsson, T.; Flach, C.; Mendelsohn, R.; Falkowski, P. G. Biological Control of Aragonite Formation in Stony Corals. *Science* **2017**, *356*, 933−938.
(70) Weiner, S.; Levi-Kalisman, Y.; Raz, S.; Addadi, L. Biologically Formed Amorphous Calcium Carbonate. *Connect. Tissue Res.* **2003**, *44*, 214−218.
(71) Nakahara, H. Nacre formation in bivalve and gastropod molluscs. In *Mechanisms and Phylogeny of Mineralization in Biological Systems*; Suga, S., Nakahara, H., Eds.; Springer-Verlag: Berlin, 1991; Chapter 4.2, pp 343−350.
(72) Ajili, W.; Tovani, C. B.; Fouassier, J.; de Frutos, M.; Laurent, G. P.; Bertani, P.; Djediat, C.; Marin, F.; Auzoux-Bordenave, S.; Azaïs, T.; Nassif, N. Inorganic phosphate in growing calcium carbonate abalone shell suggests a shared mineral ancestral precursor. *Nat. Commun.* **2022**, *13*, 1496.
(73) Veis, A.; Sfeir, C.; Wu, C. B. Phosphorylation of the proteins of the extracellular matrix of mineralized tissues by casein kinase-like activity. *Crit. Rev. Oral Biol. Med.* **1997**, *8*, 360−379.
(74) George, A.; Veis, A. Phosphorylated proteins and control over apatite nucleation, crystal growth, and inhibition. *Chem. Rev.* **2008**, *108*, 4670−4693.
(75) Borbas, J. E.; Wheeler, A. P.; Sikes, C. S. Molluscan shell matrix phosphoproteins: Correlation of degree of phosphorylation to shell mineral microstructure and to in vitro regulation of mineralization. *J. Exp. Zool.* **1991**, *258*, 1−13.
(76) Du, H.; Steinacher, M.; Borca, C.; Huthwelker, T.; Murello, A.; Stellacci, F.; Amstad, E. Amorphous $CaCO_3$: Influence of the formation time on its degree of hydration and stability. *J. Am. Chem. Soc.* **2018**, *140*, 14289−14299.

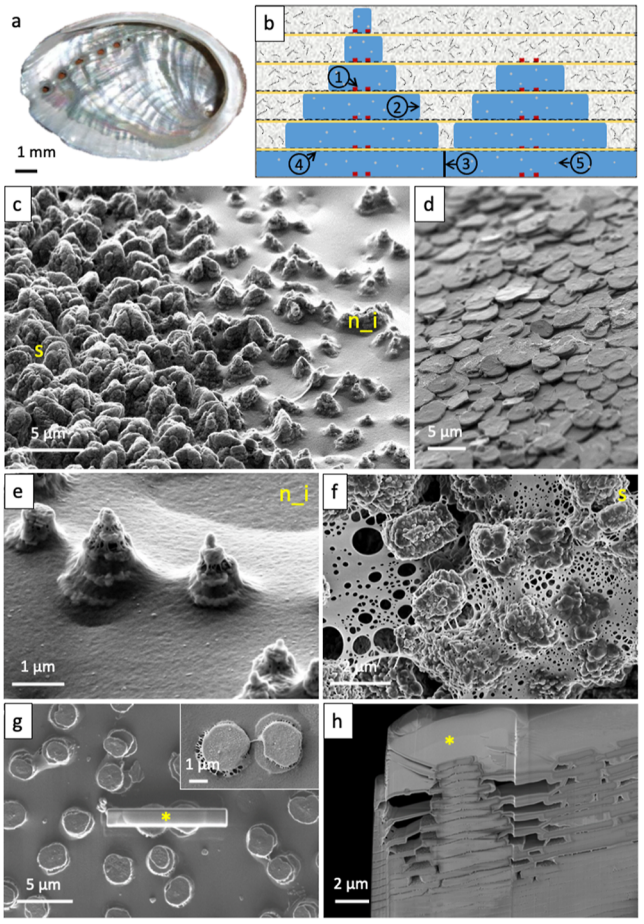

Figure 1. (a) Picture of one-year-old *H. tuberculata* shell showing the iridescent nacre (b) identification of the different possible organo–mineral interfaces in growing nacre according to the latest available published data including the Olson model.[32] (1): Within the central nucleation zone of the tablets; (2): between the lateral mineral face and the fibroin silk gel during the lateral growth; (3): between the two lateral mineral faces and into the intertabular matrix once the tablets lateral expansion is achieved; (4): between the longitudinal mineral surface and the interlamellar organic sheets; (5): within the tablets between the organic inclusions and the mineral bulk. Mineral bridges are not represented in this scheme. (c–h) FEG-SEM observations of (c) a close-up of the spherulitic part (noted s) to immature nacre (noted n_i) transition; (d) mature nacre (n_m) characterized by adjacent aragonite tablets; (e) columnar arrangement in young immature nacre region (adjacent to the spherulitic area) surrounded by a dense organic matrix; (f) spherulitic aragonite crystals surrounded by a loose organic membrane; (g) top view of growing aragonite tablets with the selected area shown by Platinum coating (*). Inset: higher magnification of the selected area which consists of 2 columns; (h) the resulting Pt coated (*) FIB thin section.

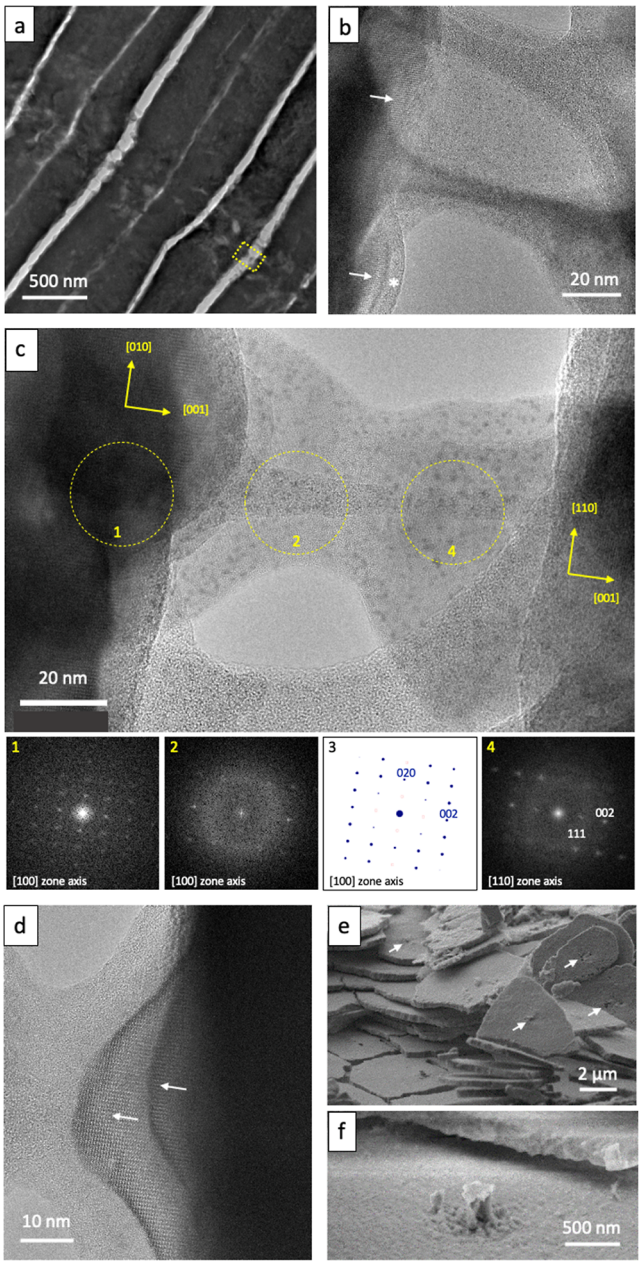

Figure 3. HR-TEM observations of (a) the central defects region, (b,c) at higher magnification highlighting the interlamellar bridges where (c) is the zone marked by the yellow-dotted rectangle in (a) with Fast-Fourier Transform (FFT) performed on selected areas (yellow dotted circles) showing the presence of both aragonite (1,2 along [100] zone axis according to simulation 3 and 4 along [110] direction) and amorphous phases (2,4) in the bridging structure. White arrows in (b,d) point to the aragonite [001] crystallographic direction (*c*-axis) inside mineral protuberance and the white star in (b) to an amorphous layer. (e,f) SEM-FEG observations of (e) stripped nacre tablets where the white arrows indicate defects or protuberances at the center of the tablets and of (f) a protuberance at higher magnification.

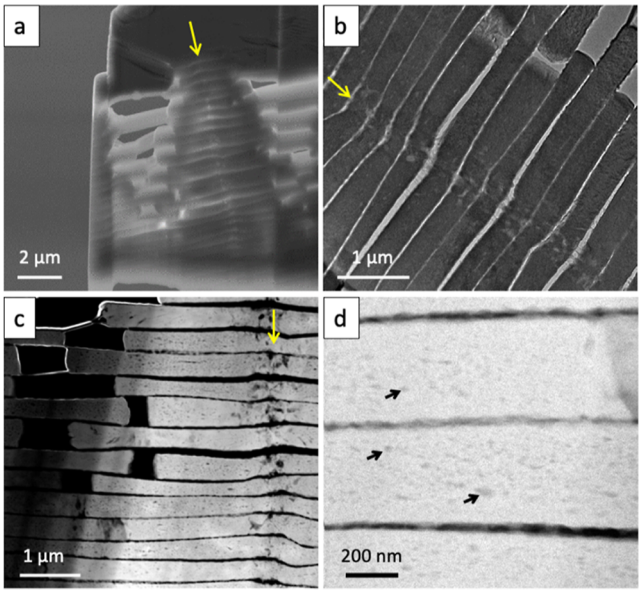

Figure 2. (a) SEM-FEG, (b) Brightfield TEM and (c) STEM HAADF images of the FIB section with a focus on the aligned defects (direction of alignment is materialized by a yellow arrow). (d) STEM HAADF image at higher magnification of one tablet. Black arrows indicate typical nanometer-sized "defects" or inclusions within the aragonite tablet.

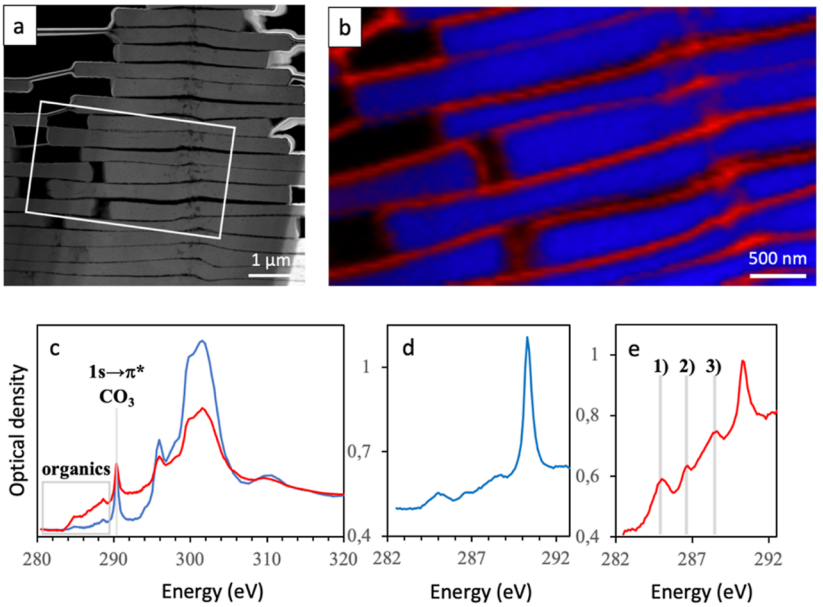

Figure 4. (a) Area of the FIB section investigated by STXM is marked with the white rectangle. (b) Resulting STXM map where mineral and organic regions are colored in blue and red, respectively. (c) Typical XANES spectra found in the mineral bulk (blue) and in the interlamellar region (red). The peak at 290.3 eV corresponding to 1s → π^* electron transitions in carbonates is shown by a gray vertical line. The spectral area where the 1s → π^* electron transitions in organic functional groups are found is highlighted by a grey rectangle. (d,e) Close-up of the two typical XANES spectra in the 280−290 eV region. Vertical lines named (1−3) are at 285.1, 286.7 eV and between 288.2 and 288.6 eV, respectively.

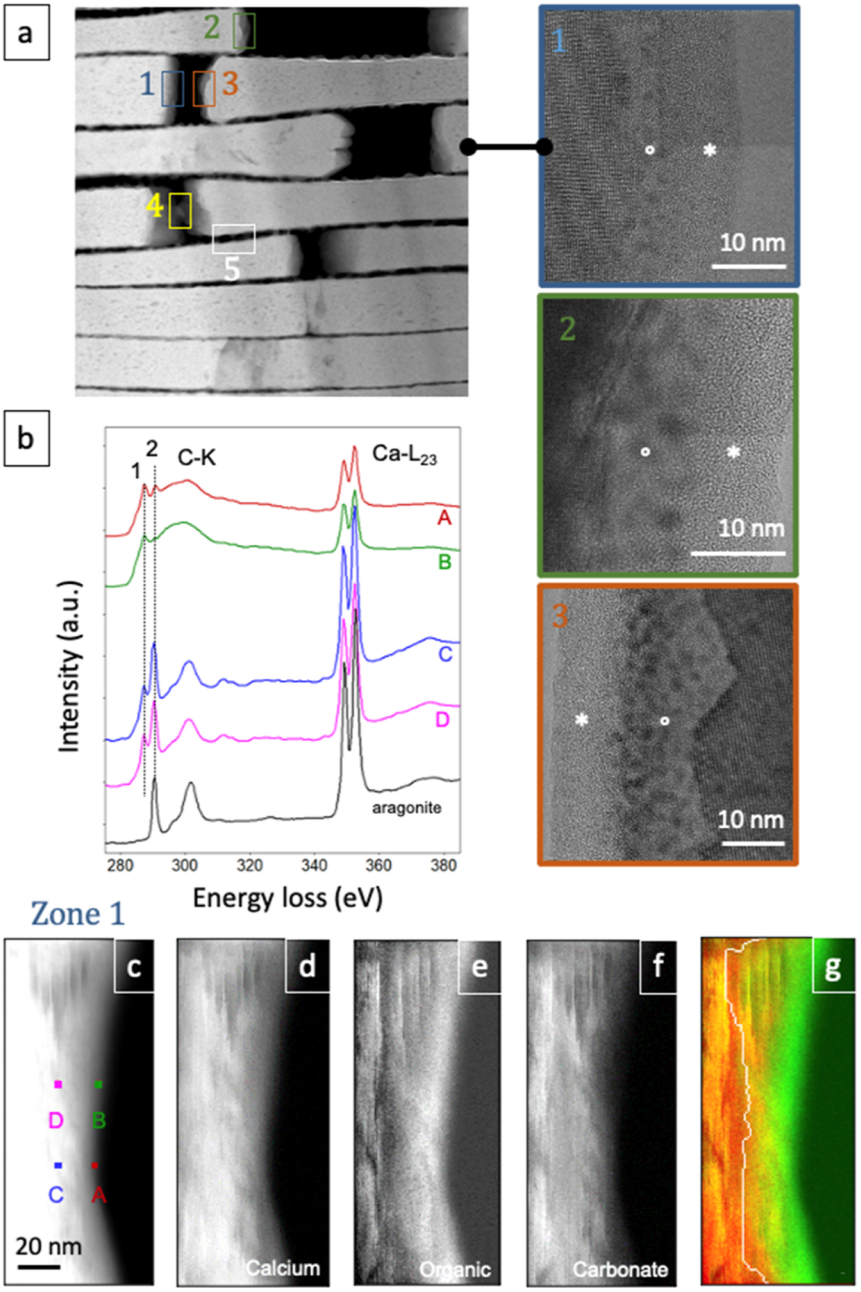

Figure 5. (a) STEM HAADF image of the investigated zones (denoted 1, 2, 3, 4, and 5). HR-TEM observations of zone 1 (blue), zone 2 (green), and zone 3 (orange). The zones 1, 4, and 5 were thereafter analyzed by EELS. (b) Typical EEL spectra acquired at different positions on the lateral growing zone 1 in (a) for the carbon K-edge and calcium L_{23}-edge. On the carbon edge, two peaks were detected at 287 and 290 eV associated with the presence of organic species (peak 1) and carbonate (peak 2), respectively. (c) STEM-HAADF image of the investigated region. A and B are at the edges, C and D are in the interior. (d–f) EELS maps corresponding to the distribution of organic species, carbonate, and calcium deduced from their respective edge signals. (g) Color composite images obtained from the individual maps (e,f) showing the relative abundances of organic species (in green) compared to carbonate (in red). The white line in (g) corresponds to the detection limit of EELS signal due to sample thickness.